

Lanthanides: new metallic cathode materials for organic photovoltaic cells

Cite this: *Phys. Chem. Chem. Phys.*, 2013, **15**, 13052

Maxim P. Nikiforov,^{†*a} Joseph Strzalka,^b Zhang Jiang^b and Seth B. Darling^{*ac}

Organic photovoltaics (OPVs) are compliant with inexpensive, scalable, and environmentally benign manufacturing technologies. While substantial attention has been focused on optimization of active layer chemistry, morphology, and processing, far less research has been directed to understanding charge transport at the interfaces between the electrodes and the active layer. Electrical properties of these interfaces not only impact efficiency, but also play a central role in stability of organic solar cells. Low work function metals are the most widely used materials for the electron transport layer with Ca being the most common material. In bulk heterojunction OPV devices, low work function metals are believed to mirror the role they play in OLEDs, where such metals are used to control carrier selectivity, transport, extraction, and blocking, as well as interface band bending. Despite their advantages, low work function materials are generally prone to reactions with water, oxygen, nitrogen, and carbon dioxide from air leading to rapid device degradation. Here we discuss the search for a new metallic cathode interlayer material that increases device stability and still provides device efficiency similar to that achieved with a Ca interlayer.

Received 12th June 2013,
Accepted 17th June 2013

DOI: 10.1039/c3cp52327f

www.rsc.org/pccp

Introduction

Organic photovoltaics (OPVs) offer the prospect of an inexpensive, scalable, and environmentally benign energy technology.^{1,2} Bulk heterojunction (BHJ) solar cells, representing the most common class of OPV devices, have recently demonstrated a remarkable increase of power conversion efficiency. Five functional layers: current collector, hole-transport layer, active layer, electron-transport layer, and current collector, comprise a BHJ solar cell (Fig. 1A). While extensive research has been directed toward optimization of active layer chemistry,³ morphology,^{4,5} and processing,⁶ significantly less attention has been paid to understanding electron and hole transport at the interface between the current collectors and the active layer. Electrical properties of these interfaces not only significantly influence efficiency of the device,^{7–9} but also affect stability of organic solar cells.^{10–12} On the anode side, poly(3,4-ethylenedioxythiophene) poly(styrenesulfonate) (PEDOT:PSS), the typical hole-transport material used in organic solar cells,

is infamous for its acidity,^{13,14} water absorption,¹⁵ as well as instability towards PSS decomposition.¹³ Such behavior leads to accelerated degradation of the active layer and the current collector.¹¹ New anodic materials, such as WO_x, MoO_x, VO_x have been introduced as a replacement for PEDOT:PSS.^{16,17} On the cathode side, low work function metals are the most widely used materials for the electron transport layer (ETL)^{9,18,19} with Ca being the most common material. In BHJ OPV devices, low work function metals are believed to play the same (though inverted) role they play in OLEDs, where such metals are used to control carrier selectivity, transport, extraction, and blocking, as well as interface band bending.⁹ Despite their numerous benefits, low work function materials are usually prone to reactions with water, oxygen, nitrogen, and carbon dioxide from air resulting in fast degradation of the device due to cathode corrosion. This paper presents a search for a new metallic cathode interlayer material that provides device efficiency similar to that achieved with a Ca interlayer while increasing stability of the device.

Taking into account chemical properties of Ca we focused our search on Group 2 metals (Ca, Sr, Ba), Sc, and lanthanides (La, Ce, Nd, Eu, Gd, Tb, Yb) (Fig. 1C). Chemical properties of the elements guided the choice of metals: (1) chemical reactivity of lanthanides and magnesium, the least reactive metal of Group 2 metals, with oxygen and water is similar;²⁰ (2) Group 2 metals as well as lanthanides tarnish because of surface oxidation and slow reaction with cold water; (3) reduction–oxidation (Ln/Ln³⁺)

^a Center for Nanoscale Materials, Argonne National Laboratory, 9700 S. Cass Avenue, Lemont, Illinois 60439, USA. E-mail: maximnik@gmail.com, darling@anl.gov; Fax: +1 630-252-4646; Tel: +1 630-252-4580

^b X-ray Science Division, Argonne National Laboratory, Lemont, Illinois, USA

^c Institute for Molecular Engineering, The University of Chicago, Chicago, Illinois, USA

[†] HGST, 3403 Yerba Buena Rd., San Jose, CA.

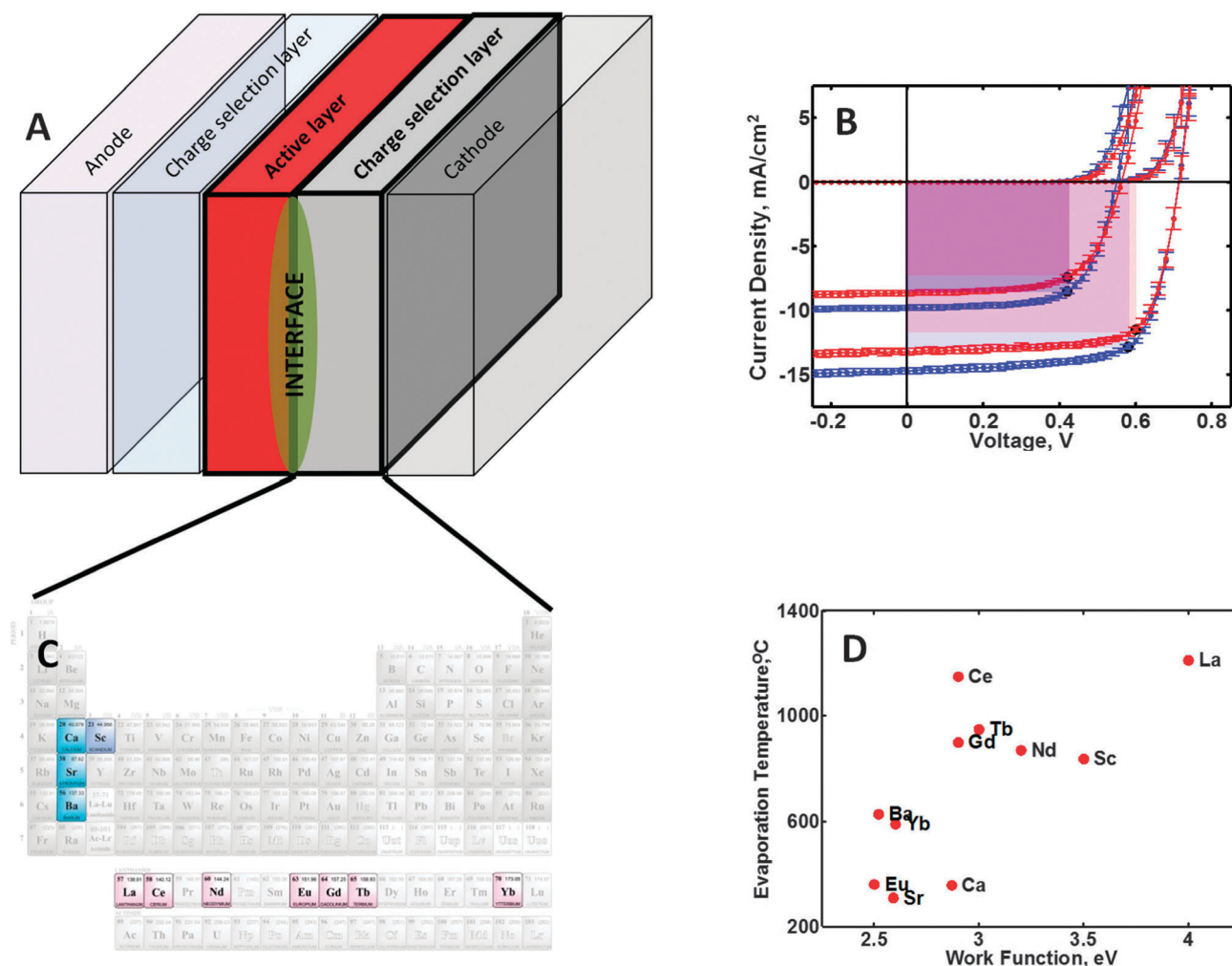


Fig. 1 (A) Solar cell layer structure schematic. (B) Average J - V curves for P3HT:PC₆₁BM- and PTB7:PC₇₁BM-based devices with Ca (blue curves) and La (red curves) charge selection layers. (C) List of metals used for cathodic charge selection layers. (D) Evaporation temperatures and work functions for the metals used as charge selection layers.

Table 1 Physico-chemical properties of metals used as cathode interlayers

Atomic number	Element symbol	Red/Ox potential Ln/Ln ³⁺ , M/M ²⁺ (V, SHE) ²⁰	Oxidation states ²⁰	Work function (eV)	Evaporation temperature (°C)	Critical angle ^a (degrees), ²¹
20	Ca	-2.87	2	2.87	357	0.199
21	Sc	-2.00	3	3.50	837	0.267
38	Sr	-2.89	2	2.59	309	0.235
56	Ba	-2.90	2	2.52	627	0.264
57	La	-2.38	2(n), 3, 4	4.00	1212	0.349
58	Ce	-2.34	2(n), 3, 4	2.90	1150	0.365
59	Pr	-2.35	2(n), 3, 4			
60	Nd	-2.32	2(n), 3	3.20	871	0.361
61	Pm	-2.29	3			
62	Sm	-2.30	2(n), 3			
63	Eu	-1.99	2, 3	2.50	360	0.305
64	Gd	-2.28	3	2.90	900	0.361
65	Tb	-2.31	3, 4	3.00	950	0.377
66	Dy	-2.29	2(n), 3			
67	Ho	-2.33	3			
68	Er	-2.32	3			
69	Tm	-2.32	2(n), 3			
70	Yb	-2.22	2, 3	2.60	590	0.354
71	Lu	-2.30	3			

^a For photon energy 7.35 keV.

potential indicates decreased reactivity of lanthanides in comparison with that of calcium (Table 1).

Experimental

Materials

PTB7 (poly[[4,8-bis[(2-ethylhexyl)oxy]benzo[1,2-*b*:4,5-*b'*]dithiophene-2,6-diyl][3-fluoro-2-[(2-ethylhexyl)carbonyl]thieno[3,4-*b*]thiophene-diyl]]) polymer was purchased from 1-Material (Québec, Canada). [6,6]-Phenyl-C₇₁-butyric acid methyl ester (PC₇₁BM, >99%) was obtained from American Dye Source. Metals (Ca, Sr, Ba, Sc, La, Ce, Nd, Eu, Gd, Tb, Yb, purity >99%), 1,8-diiodooctane (DIO) (98%, contains copper as stabilizer), 1,2-dichlorobenzene (DCB, 99% purity anhydrous), and Plexcore PV 1000 ink were purchased from Aldrich. Poly(3,4-ethylenedioxythiophene) poly(styrenesulfonate) (PEDOT:PSS) was obtained from Heraeus (Clevios P VP AI 4083). Indium tin oxide (ITO)-coated glass substrates were supplied by Delta Technologies, Ltd. (25 Ω sq⁻¹). All materials were used without further purification.

Grazing incidence wide-angle X-ray scattering (GIWAXS)

GIWAXS measurements were performed at the 8-ID-E beamline²² at the Advanced Photon Source (APS), Argonne National Laboratory using X-rays with a wavelength of $\lambda = 1.6868$ Å and a beam size of ~ 100 μ m (h) \times 50 μ m (v). Samples for GIWAXS experiments reproduced layer stacking of OPV devices (glass/ITO/PEDOT:PSS/P3HT:PC₆₁BM/Me/Al, where Me = Ca, Sr, Ba, Sc, La, Ce, Nd, Eu, Gd, Tb, Yb), OPV devices without top electrode (glass/ITO/PEDOT:PSS/P3HT:PC₆₁BM), and metals on glass (glass/Me/Al, where Me = Ca, Sr, Ba, Sc, La, Ce, Nd, Eu, Gd, Tb, Yb). The thickness of Al layer for GIWAXS measurements was reduced to 20 nm in comparison with 50 nm Al layer used for device preparation. The same layer deposition conditions were used for preparation of OPV devices and samples for GIWAXS. The thickness of Al layer was reduced to 20 nm from 50 nm used in the devices to improve X-ray transparency of the Al films. A Pilatus 1M-F pixel array detector (Dectris) was used to capture the X-ray scattering patterns. The distance between detector and the samples was 204.152 mm. GIWAXS patterns were recorded at an incidence angle of 0.38° in order to penetrate the top Al and Me layers, with two exposures at different detector vertical positions. After flatfield correction for detector nonuniformity, the images are combined to fill in the gaps for rows of inactive pixels at the borders between modules, leaving dark only the columns of inactive pixels at the center of the images. Using the GIXSGUI²³ package for Matlab (Mathworks), data are corrected for X-ray polarization, detector sensitivity, and geometrical solid-angle before mapping from pixel space into the (*q*, α) coordinate system, where α is the polar angle in the detector plane, or the tilt angle with respect to the out-of-(substrate)-plane direction. This transforms the inactive columns of pixels into the arcing feature that appears white in Fig. 3A. This representation facilitates comparison of the GIWAXS patterns observed for the different samples in the study, and especially the Gaussian fit of the (200) P3HT peak, which was performed using an automated in-house written MATLAB script.

Device fabrication

Detailed description of the device fabrication procedures can be found elsewhere.^{12,24} The PEDOT:PSS hole-transport layer was prepared by spin coating at 1000 rpm in ambient conditions on clean 1 in. \times 1 in. ITO-coated glass substrates followed by annealing in a nitrogen-filled glove box at 150 °C for 15 min. This procedure typically results in a 50 nm thick PEDOT:PSS layer. For PTB7:PC₇₁BM-based devices, the active layer was spin coated from PTB7-based solution at 1000 rpm. The solutions used for active layer preparation contained PTB7, PC₇₁BM, DIO, and DCB. To prepare 1 mL of solution, 10 mg of PTB7 and 15 mg of PC₇₁BM were dissolved in DCB:DIO mixture (3% DIO by volume). For P3HT:PC₆₁BM-based devices, the photoactive layer consisting of P3HT:PC₆₁BM composite was obtained by spin-coating Plexcore PV 1000 ink at 800 rpm on the PEDOT:PSS-modified ITO substrates in an integrated glove box system equipped with a thermal evaporator followed by annealing of the wafers at 120 °C for 5 min under nitrogen. After deposition of hole-transport and active layers, an electron-transport layer was deposited using thermal evaporation of Me (Ca, Sr, Ba, Sc, La, Ce, Nd, Eu, Gd, Tb, Yb) (50 nm) and Al (50 nm) layers under vacuum (3×10^{-6} mbar or better). Samples with only Ca and La cathode interlayers were prepared for PTB7:PC₇₁BM-based devices.

Device characterization

The active device area was limited to 4.87 mm² by a shadow mask. Current-voltage (*I*-*V*) curves were recorded using a Keithley 2420 source-measure unit. The photocurrent was measured under AM 1.5 G illumination at 100 mW cm⁻² under a Newport Oriel Solar Simulator with a 300 Watt Xenon source and 2 in. \times 2 in. illuminated area. Prior to each measurement, the light intensity was adjusted to ensure constant repeatable light power density using NREL-calibrated photodiodes. Standard solar cell parameters, such as power conversion efficiency, fill factor, and short-circuit current, were calculated from *J*-*V* curves of the solar cell under illumination using conventional procedures. Three to eight devices were measured for each experimental condition.

Results and discussion

To test the effect of the metal interlayer on solar cell performance we initially focused on the classic P3HT:PC₆₁BM-based system (ITO/PEDOT:PSS/P3HT:PC₆₁BM/metal/Al)²⁵ (Fig. 1A). Cathode interlayer thickness remained constant (50 nm) for all OPV devices. During deposition of the cathode interlayer, various physical and chemical processes, such as metal diffusion into the organic layer,²⁶ band bending,²⁷ chemical reactions,²⁶ interfacial energy barrier formation, *etc.*, occur at the interface between the cathode and the active layer. The metals chosen for investigation as cathode interlayers cover a wide range of evaporation temperatures, work functions, and reduction-oxidation (Red/Ox) potentials (Fig. 1D and Table 1). This diversity of properties allows us to test several

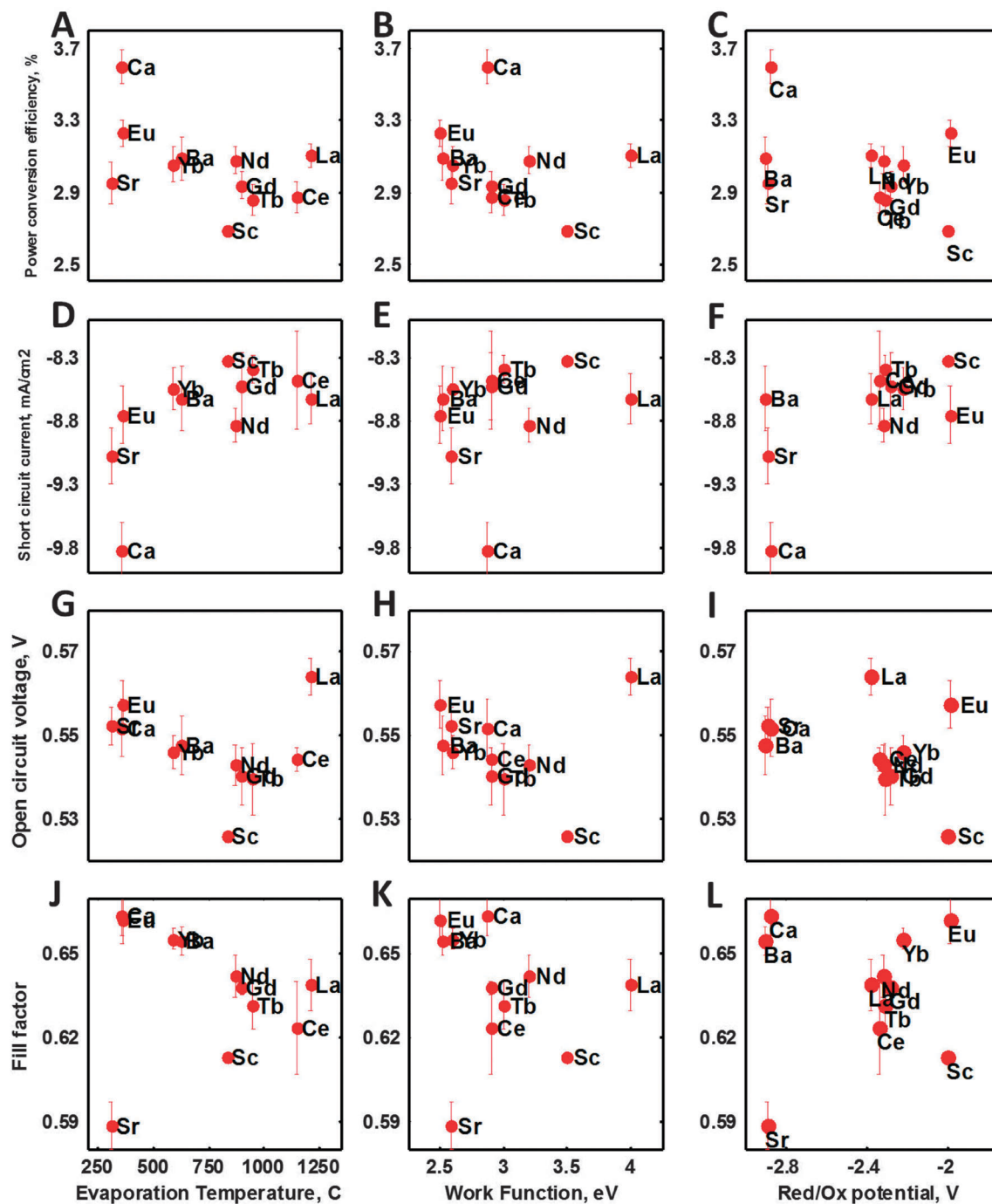


Fig. 2 Parameters (power conversion efficiency (A–C), short circuit current (D–F), open circuit voltage (G–I), fill factor (J–L)) of P3HT:PC61BM-based solar cells with different cathode interlayers. The first, second, and third columns show dependence of solar cell parameters on metal evaporation temperature (A, D, G, and J), metal work function (B, E, H, and K), and Red/Ox potential (C, F, I, and L) of the metal.

hypotheses about the processes happening at the cathode-active layer interface:

1. If metal diffusion alone controls the device performance, then correlation between device parameters and metal evaporation temperatures is expected.

2. If alignment of energy levels at the interface alone controls the device performance, then correlation between device parameters and metal work functions is expected because of

the work function dependence of current flowing through metal–semiconductor contacts.²⁸

3. If chemical reaction at the interface alone controls the device performance then correlation between device parameters and red-ox potential of metals is expected.

Fig. 2A–D show weak correlation between evaporation temperature and power conversion efficiency, short circuit current, as well as fill factor. At the same time, almost no correlation is evident

between solar cell parameters and the work function of the metal layer (Fig. 2E–H) or the reduction–oxidation potential (Fig. 2I–L). The explanation for such behavior can be concurrent action of several drivers, such as diffusion of metal into the polymer layer,^{29,30} alignment of energy levels^{31,32} or band bending at the interface,^{33,34} and chemical reactions.^{30,33,34}

To reveal molecular-scale changes in the structure of the active layer (P3HT:PC₆₁BM), we apply grazing incidence wide-angle X-ray scattering (GIWAXS). Comparison of GIWAXS data

from the complete solar cell (ITO/PEDOT:PSS/P3HT:PC₆₁BM/metal (50 nm)/Al (20 nm)) and the solar cell without top electrode (ITO/PEDOT:PSS/P3HT:PC₆₁BM) allows for quantification of changes in the active layer resulting from the metal deposition process. Fig. 3A shows an example of the X-ray scattering pattern collected from a solar cell with a La cathode interlayer, a solar cell without the top electrode from the same wafer, a lanthanum film with 50 nm thickness deposited on silicate glass, and an ITO/PEDOT:PSS sample. Comparison of diffractograms from these four

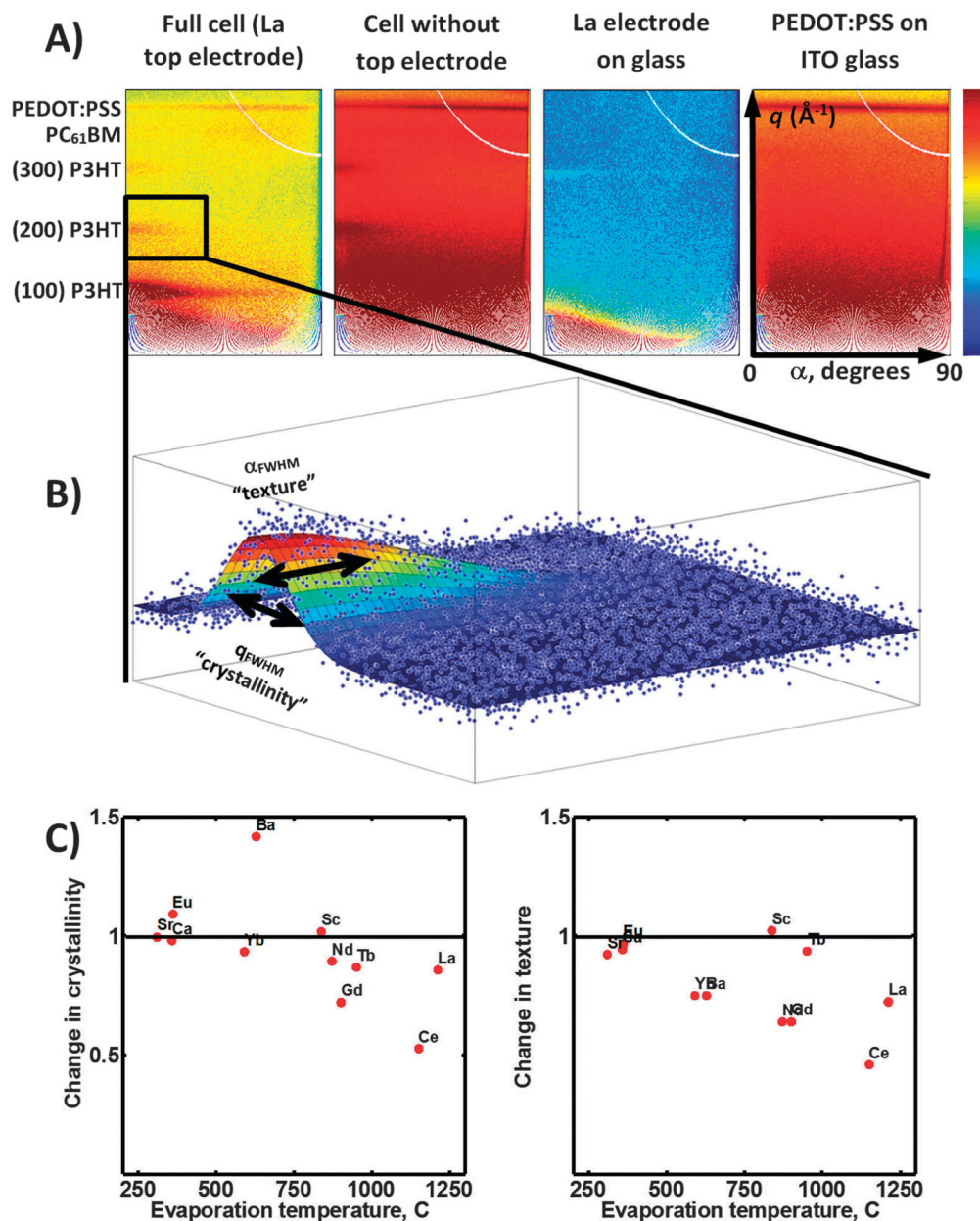


Fig. 3 (A) X-ray scattering (GIWAXS) maps q (\AA^{-1}) vs. α (tilt with respect to the out-of-(substrate)-plane direction) of the full cell (ITO/PEDOT:PSS/P3HT:PC₆₁BM/La/Al), the cell without top electrode (ITO/PEDOT:PSS/P3HT:PC₆₁BM), the metal electrode on glass (silicate glass/La/Al), and the PEDOT:PSS layer on ITO glass (ITO/PEDOT:PSS). (B) Selected area of X-ray scattering map around the (200) P3HT peak around $q = 0.8 \text{ \AA}^{-1}$. Blue points are experimental data, curved surface is a least square fit of the data using a 3D Gaussian. Full width at half maximum (FWHM) in q and α directions are measures of crystallinity (q) and texture (α). (C) Change in crystallinity (the ratio of q_{FWHM} for cell without top electrode and complete cell) as a function of cathode interlayer evaporation temperature (change in crystallinity < 1 denotes decrease in crystallinity of the P3HT phase). Change in texture (the ratio of α_{FWHM} for cell without top electrode and complete cell) as a function of cathode interlayer evaporation temperature (change in texture < 1 denotes decrease in texture of the P3HT phase).

samples (Fig. 3A) allows for attribution of the peaks appearing on the diffractogram to metal, active layer, and PEDOT:PSS phases. The incident angle for the X-ray beam was 0.38 degrees (greater than the critical angle of all metals of interest (Table 1)), assuring X-ray penetration through the metal films. The width of the X-ray peak (full width at half maximum (FWHM)) in the q direction is correlated with the crystallinity of the material through Sherrer's formula. The width of the X-ray peak in the α direction provides information about the texture of the sample. At zero α , crystal planes that are parallel to the sample surface are in Bragg condition; at α equals 90 degrees, crystal planes that are perpendicular to the sample surface are in Bragg condition. Thus, the width of the diffraction peak in the α direction is a measure of out-of-plane material texture (smaller width corresponds to stronger texture). In order to quantify crystallinity and texture, the (200) peak of P3HT was chosen because this peak does not overlap with any of the peaks coming from metals or PEDOT:PSS. This peak has been fitted to a 3-dimensional Gaussian profile (eqn (1)):

$$I(q, \alpha) = a \exp \left(- \frac{[(q - q_0) \cos(A) + (\alpha - \alpha_0) \sin(A)]^2}{2 \times q_{\text{FWHM}}^2} - \frac{[(q - q_0) \sin(A) + (\alpha - \alpha_0) \cos(A)]^2}{2 \times \alpha_{\text{FWHM}}^2} \right) \quad (1)$$

where a is a peak amplitude, q is a momentum transfer vector (variable parameter), q_0 is a momentum transfer vector that corresponds to reflection from a particular set of planes in the sample ((200)-family of planes in P3HT in our case), α is a tilt angle with respect to the out-of-(substrate)-plane, α_0 is an angle of preferred orientation of the crystallites in the sample (~ 0 degrees in our case indicating strong orientation of (200) planes parallel to the sample surface), q_{FWHM} is a full-width at half-maximum of the (200) P3HT diffraction peak in the q direction, α_{FWHM} is a full-width at half-maximum of the (200) P3HT diffraction peak in the α direction, A is a tilt angle of the (200) P3HT diffraction peak in the q - α plane.

Fig. 3B shows a sample fit of the X-ray peak using eqn (1). The X-ray peak fitting procedure was performed for all cathode interlayers. The change in crystallinity of P3HT caused by cathode deposition can be determined by comparing crystallinity ($q_{\text{FWHM}}(\text{no metal})/q_{\text{FWHM}}(\text{metal})$) and texture ($\alpha_{\text{FWHM}}(\text{no metal})/\alpha_{\text{FWHM}}(\text{metal})$) of the active layer under the electrode with crystallinity and texture of the as-prepared sample. An increase in FWHM of the X-ray peak indicates a decrease in crystallinity or sample texture. Fig. 3C shows that crystallinity of the P3HT as well as degree of texturing decreases upon deposition of all metals except Ba and Eu. Correlation between crystallinity/texturing and evaporation temperature is evident. Such behavior is likely guided by energy dissipation at the active layer-metal interface. Metals with higher evaporation temperature deliver more thermal energy to the interface. Recrystallization of the polymer is expected when extra thermal energy is added to the system. In P3HT:PC₆₁BM blends, re-crystallization, which typically improves texture,⁴⁶ is often accompanied by phase separation.⁴⁷

The decrease of crystallinity and texture in our experiments (Fig. 3C) indicates disturbance of the active layer during electrode deposition. Taking into account that diffusion of Al into the P3HT:PC₆₁BM layer has been observed,⁴⁸ diffusion of the metal atoms into the active layer is a likely cause for decrease in polymer order inside the active layer in our experiment. For accurate description of electronic processes in BHJ OPV devices, band bending at the active layer-metal interface associated with the finite width of the interface needs to be taken into account, while flat band alignment of energy levels is typically assumed for OPVs.

Peculiar interplay between energy level alignment, band bending, interface diffusion, and interface reactions results in the difference in power conversion efficiency of around 15% for the devices with Ca and La cathode interlayers (Fig. 1B and 2A). Common theory based on band alignment at an infinitely sharp metal-semiconductor interface²⁸ predicts significant decrease of power conversion efficiency (PCE) of the device due to energy barrier formation at the cathode interface for high work function metals. More than a 50% drop in PCE has been reported upon the change of cathode interlayer from Ca (2.87 eV) to Al (4.28 eV) and Ag (4.26 eV).¹⁹ Following this band alignment framework, devices with a calcium interlayer should not have an energy barrier at the cathode interface, while devices with a lanthanum, aluminum, or silver interlayer should have a small barrier because the work function of La, Al, and Ag is typically larger than the PC₆₁BM LUMO energy (Table 2 and Fig. 4).

Table 2 Energies of HOMO, LUMO levels for active layer materials

Compound	HOMO (eV)	LUMO (electron affinity) (eV)	E_g	Ref.
PC ₆₁ BM	5.79–5.93	3.7–4.3		35–38
PC ₇₁ BM	5.87	3.91		38
P3HT			1.7–2.1	39–42
P3HT		3.2–3.5		39,43,44
PTB7	5.15	3.31		45

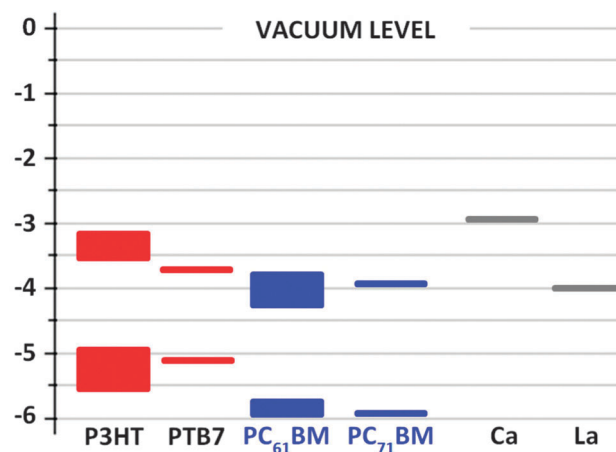


Fig. 4 Literature data on work functions of cathode interlayers (Ca, La) as well as energies of the HOMO and LUMO levels for active layer materials (P3HT, PTB7, PC₆₁BM, PC₇₁BM). Energy bands present ranges for energy level position reported in the literature (Table 2).

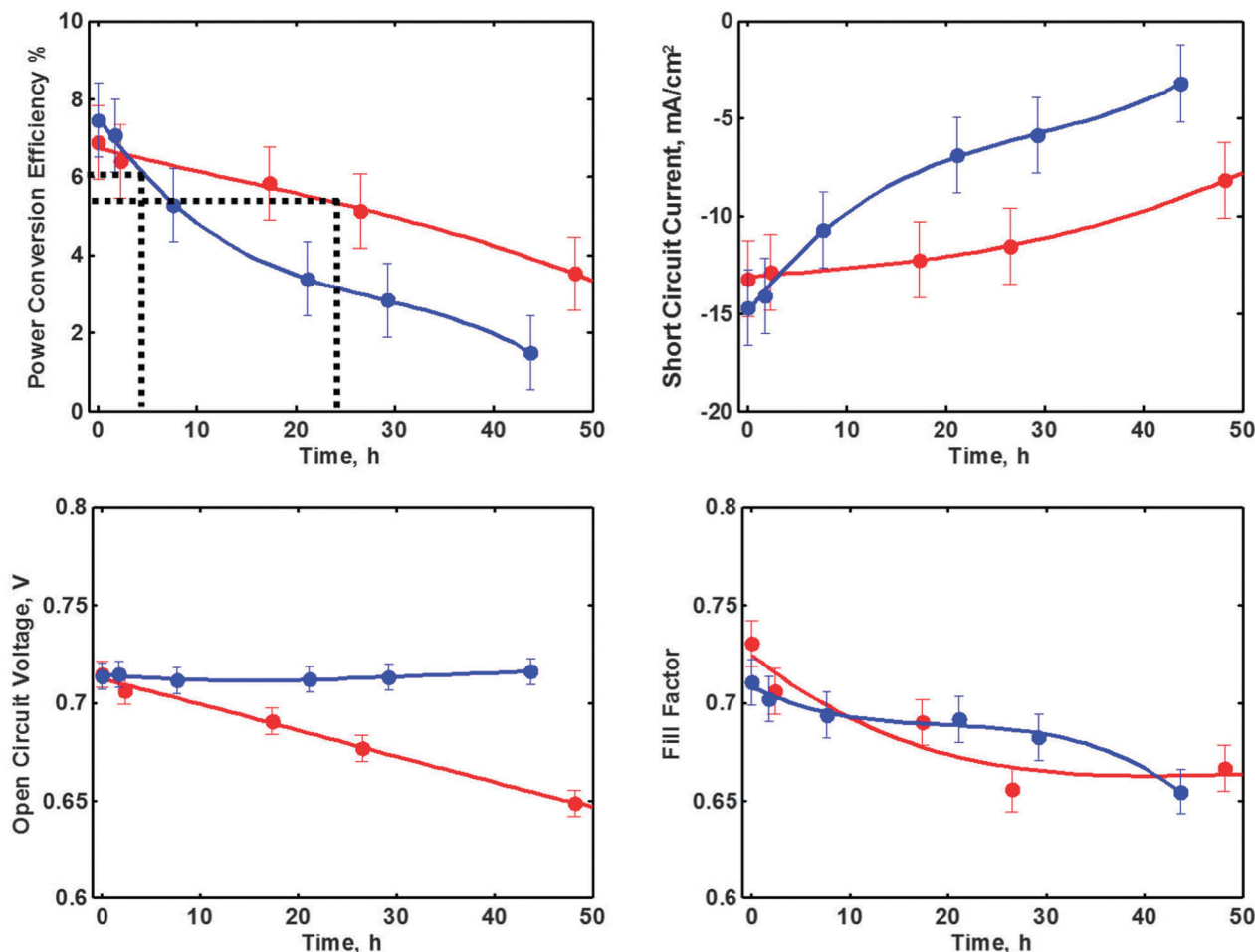


Fig. 5 Ambient degradation of optoelectrical characteristics for PTB7:PC₇₁BM-based solar cells (ITO/PEDOT:PSS/PTB7:PC₇₁BM/(La or Ca)/Al) without encapsulation. Data for Ca (La) cathode interlayer are shown in blue (red). Lines are a guide to the eye.

In turn, the energy barrier at the cathode interface should significantly decrease power conversion efficiency of the solar cell. Our device measurements show only a small (15%) decrease in PCE suggesting that the assumption of an infinitely sharp metal–polymer interface does not hold. Decrease of P3HT crystallinity and texture upon deposition of metals discovered during GIWAXS measurements also supports the hypothesis of cathode metal diffusion into the active layer.

The studies of the P3HT:PC₆₁BM, photovoltaic system²⁵ allowed us to identify lanthanum as a promising candidate for the cathode interlayer, which maintains device efficiency on par with Ca-based devices and provides a possibility of improved degradation performance. Rapid development in the OPV field calls for new materials with improved device performance, and the PTB7:PC₇₁BM system has exhibited among the highest reported power conversion efficiencies to date.^{25,45} Fig. 1B shows the difference in current–voltage characteristics for as prepared solar cells with P3HT:PC₆₁BM and PTB7:PC₇₁BM active layers. Because of its superior performance, the PTB7:PC₇₁BM system was chosen for degradation studies. Fig. 5 shows the decrease of power conversion efficiency, short circuit current, open circuit voltage and fill factor

for solar cells with Ca (blue) and La (red) cathode interlayers having no encapsulation. The time required for 20% decrease of solar cell parameters is a commonly accepted measure of device degradation.⁴⁹ According to this metric, device degradation time for the solar cell with a Ca cathode interlayer is about 5 hours, while degradation time for the device with a La cathode interlayer is about 24 hours. Devices were stored in the dark under ambient atmosphere except during measurement in the solar simulator. The change of cathode interlayer from Ca to La slows degradation by more than four times. Thus, our experimental results suggest that for the PTB7:PC₇₁BM system the degradation rate is proportional to chemical reactivity of the cathode.

Conclusions

In conclusion, we found that crystallinity of conjugated polymer and orientation of polymer crystallites inside the active layer decreases due to cathode metal diffusion into the active layer. Contrary to the common belief, optoelectronic function of the devices does not depend strongly on the work function of the metallic cathode interlayers (lanthanides and Group 2 metals) in

the P3HT:PC₆₁BM system. Lanthanum is a promising cathode interlayer material for increasing lifetime of BHJ OPV devices because PTB7:PC₇₁BM-based (unencapsulated) devices, which use lanthanum as a cathode interlayer, show more than four times longer lifetime than devices using calcium as a cathode interlayer, while demonstrating relatively small (15–20%) decrease in power conversion efficiency.

Acknowledgements

This work was performed, in part, at the Center for Nanoscale Materials, a U.S. Department of Energy, Office of Science, Office of Basic Energy Sciences User Facility under Contract No. DE-AC02-06CH11357. Use of the Advanced Photon Source (APS) at Argonne National Laboratory was supported by the U.S. Department of Energy, Office of Science, Office of Basic Energy Sciences, under Contract No. DE-AC02-06CH11357. MPN is grateful to the Director's Fellowship Program for financial support.

Notes and references

- 1 J. Nelson, *Mater. Today*, 2011, **14**, 462–470.
- 2 D. J. Yue, P. Khatav, F. Q. You and S. B. Darling, *Energy Environ. Sci.*, 2012, **5**, 9163–9172.
- 3 Z. B. Henson, K. Mullen and G. C. Bazan, *Nat. Chem.*, 2012, **4**, 699–704.
- 4 W. Chen, M. P. Nikiforov and S. B. Darling, *Energy Environ. Sci.*, 2012, **5**, 8045–8074.
- 5 M. P. Nikiforov and S. B. Darling, *Prog. Photovoltaics*, 2012, DOI: 10.1002/pip.2217.
- 6 B. Liu, R.-Q. Peng, L.-H. Zhao, L.-L. Chua, R. H. Friend and P. K. H. Ho, *Nat. Commun.*, 2012, **3**, 1321.
- 7 E. L. Ratcliff, B. Zacher and N. R. Armstrong, *J. Phys. Chem. Lett.*, 2011, **2**, 1337–1350.
- 8 R. Steim, F. R. Kogler and C. J. Brabec, *J. Mater. Chem.*, 2010, **20**, 2499–2512.
- 9 L.-M. Chen, Z. Xu, Z. Hong and Y. Yang, *J. Mater. Chem.*, 2010, **20**, 2575–2598.
- 10 M. Jorgensen, K. Norrman, S. A. Gevorgyan, T. Tromholt, B. Andreasen and F. C. Krebs, *Adv. Mater.*, 2012, **24**, 580–612.
- 11 M. Jorgensen, K. Norrman and F. C. Krebs, *Solar Energy Mater. Solar Cells*, 2008, **92**, 686–714.
- 12 M. P. Nikiforov, J. Strzalka and S. B. Darling, *Solar Energy Mater. Solar Cells*, 2013, 36–42.
- 13 J. Y. Lee, *Synth. Met.*, 2006, **156**, 537–540.
- 14 K. W. Wong, H. L. Yip, Y. Luo, K. Y. Wong, W. M. Lau, K. H. Low, H. F. Chow, Z. Q. Gao, W. L. Yeung and C. C. Chang, *Appl. Phys. Lett.*, 2002, **80**, 2788–2790.
- 15 Y. Suh, N. Lu, S. H. Lee, W.-S. Chung, K. Kim, B. Kim, M. J. Ko and M. J. Kim, *ACS Appl. Mater. Interfaces*, 2012, **4**, 5118–5124.
- 16 J. Meyer, S. Hamwi, M. Kroeger, W. Kowalsky, T. Riedl and A. Kahn, *Adv. Mater.*, 2012, **24**, 5408–5427.
- 17 Y. C. Tseng, A. U. Mane, J. W. Elam and S. B. Darling, *Sol. Energy Mater. Sol. Cells*, 2012, **99**, 235–239.
- 18 F. Bebensee, M. Schmid, H.-P. Steinrueck, C. T. Campbell and J. M. Gottfried, *J. Am. Chem. Soc.*, 2010, **132**, 12163–12165.
- 19 M. O. Reese, M. S. White, G. Rumbles, D. S. Ginley and S. E. Shaheen, *Appl. Phys. Lett.*, 2008, **92**, 053307.
- 20 P. W. Atkins, T. L. Overton, J. P. Rourke, M. T. Weller and F. A. Armstrong, *Shriver and Atkins' Inorganic Chemistry*, Oxford University Press, 5th edn, 2010.
- 21 B. L. Henke, E. M. Gullikson and J. C. Davis, X-ray interactions: photoabsorption, scattering, transmission, and reflection at $E = 50\text{--}30\,000$ eV, $Z = 1\text{--}92$, *At. Data Nucl. Data Tables*, 1993, **54**(2), 181–342.
- 22 Z. Jiang, X. F. Li, J. Strzalka, M. Sprung, T. Sun, A. R. Sandy, S. Narayanan, D. R. Lee and J. Wang, *J. Synchrotron Radiat.*, 2012, **19**, 627–636.
- 23 Z. Jiang, GIXSGUI is available for download: <http://www.aps.anl.gov/Sectors/Sector8/Operations/GIXSGUI.html>.
- 24 Y. Liang, Z. Xu, J. Xia, S.-T. Tsai, Y. Wu, G. Li, C. Ray and L. Yu, *Adv. Mater.*, 2010, **22**, E135–E138.
- 25 M. T. Dang, L. Hirsch and G. Wantz, *Adv. Mater.*, 2011, **23**, 3597–3602.
- 26 J. Zhu, F. Bebensee, W. Hieringer, W. Zhao, J. H. Baricuatro, J. A. Farmer, Y. Bai, H.-P. Steinrueck, J. M. Gottfried and C. T. Campbell, *J. Am. Chem. Soc.*, 2009, **131**, 13498–13507.
- 27 C. G. Shuttle, R. Hamilton, B. C. O'Regan, J. Nelson and J. R. Durrant, *Proc. Natl. Acad. Sci. U. S. A.*, 2010, **107**, 16448–16452.
- 28 S. M. Sze, *Physics of semiconductor devices*, Wiley, 1981.
- 29 A. K. Mukherjee, A. K. Thakur, W. Takashima and K. Kaneto, *J. Phys. D: Appl. Phys.*, 2007, **40**, 1789–1793.
- 30 J. F. Zhu, F. Bebensee, W. Hieringer, W. Zhao, J. H. Baricuatro, J. A. Farmer, Y. Bai, H. P. Steinrueck, J. M. Gottfried and C. T. Campbell, *J. Am. Chem. Soc.*, 2009, **131**, 13498–13507.
- 31 R. J. Davis, M. T. Lloyd, S. R. Ferreira, M. J. Bruzek, S. E. Watkins, L. Lindell, P. Sehati, M. Fahlman, J. E. Anthony and J. W. P. Hsu, *J. Mater. Chem.*, 2011, **21**, 1721–1729.
- 32 C. P. Chen, T. C. Tien, B. T. Ko, Y. D. Chen and C. Ting, *ACS Appl. Mater. Interfaces*, 2009, **1**, 741–745.
- 33 W. Zhao, Y. X. Guo, X. F. Feng, L. Zhang, W. H. Zhang and J. F. Zhu, *Chin. Sci. Bull.*, 2009, **54**, 1978–1982.
- 34 X. F. Feng, W. Zhao, H. X. Ju, L. Zhang, Y. F. Ye, W. H. Zhang and J. F. Zhu, *Org. Electron.*, 2012, **13**, 1060–1067.
- 35 J. T. Bloking, X. Han, A. T. Higgs, J. P. Kastrop, L. Pandey, J. E. Norton, C. Risko, C. E. Chen, J. L. Bredas, M. D. McGehee and A. Sellinger, *Chem. Mater.*, 2011, **23**, 5484–5490.
- 36 M. C. Scharber, D. Wuhlbacher, M. Koppe, P. Denk, C. Waldauf, A. J. Heeger and C. L. Brabec, *Adv. Mater.*, 2006, **18**, 789–794.
- 37 E. T. Hoke, I. T. Sachs-Quintana, M. T. Lloyd, I. Kauvar, W. R. Mateker, A. M. Nardes, C. H. Peters, N. Kopidakis and M. D. McGehee, *Adv. Energy Mater.*, 2012, **2**, 1351–1357.
- 38 Y. J. He and Y. F. Li, *Phys. Chem. Chem. Phys.*, 2011, **13**, 1970–1983.
- 39 M. Al-Ibrahim, S. Sensfuss, J. Uziel, G. Eicke and O. Ambacher, *Solar Energy Mater. Solar Cells*, 2005, **85**, 277–283.

- 40 S. Berson, R. de Bettignies, S. Bailly, S. Guillerez and B. Jousselme, *Adv. Funct. Mater.*, 2007, **17**, 3363–3370.
- 41 D. Chirvase, Z. Chiguvare, M. Knipper, J. Parisi, V. Dyakonov and J. C. Hummelen, *J. Appl. Phys.*, 2003, **93**, 3376–3383.
- 42 M. Estrada, I. Mejia, A. Cerdeira and B. Iniguez, *Solid-State Electron.*, 2008, **52**, 53–59.
- 43 M. Y. Chang, C. S. Wu, Y. F. Chen, B. Z. Hsieh, W. Y. Huang, K. S. Ho, T. H. Hsieh and Y. K. Han, *Org. Electron.*, 2008, **9**, 1136–1139.
- 44 J. C. Nolasco, R. Cabre, J. Ferre-Borrull, L. F. Marsal, M. Estrada and J. Pallares, *J. Appl. Phys.*, 2010, **107**, 044505.
- 45 Y. Liang, Z. Xu, J. Xia, S.-T. Tsai, Y. Wu, G. Li, C. Ray and L. Yu, *Adv. Mater.*, 2010, **22**, E135–E138.
- 46 H. J. Kim, J. H. Park, H. H. Lee, D. R. Lee and J. J. Kim, *Org. Electron.*, 2009, **10**, 1505–1510.
- 47 W. R. Wu, U. S. Jeng, C. J. Su, K. H. Wei, M. S. Su, M. Y. Chiu, C. Y. Chen, W. B. Su, C. H. Su and A. C. Su, *ACS Nano*, 2011, **5**, 6233–6243.
- 48 H. J. Kim, H. H. Lee and J. J. Kim, *Macromol. Rapid Commun.*, 2009, **30**, 1269–1273.
- 49 M. O. Reese, S. A. Gevorgyan, M. Jorgensen, E. Bundgaard, S. R. Kurtz, D. S. Ginley, D. C. Olson, M. T. Lloyd, P. Moryllo, E. A. Katz, A. Elschner, O. Haillant, T. R. Currier, V. Shrotriya, M. Hermenau, M. Riede, K. R. Kirov, G. Trimmel, T. Rath, O. Inganas, F. Zhang, M. Andersson, K. Tvingstedt, M. Lira-Cantu, D. Laird, C. McGuinness, S. Gowrisanker, M. Pannone, M. Xiao, J. Hauch, R. Steim, D. M. DeLongchamp, R. Roesch, H. Hoppe, N. Espinosa, A. Urbina, G. Yaman-Uzunoglu, J.-B. Bonekamp, A. J. J. M. van Breemen, C. Girotto, E. Voroshazi and F. C. Krebs, *Solar Energy Mater. Solar Cells*, 2011, **95**, 1253–1267.